Materials & Design 268 (2026) 116439

Contents lists available at ScienceDirect

Materials & Design

journal homepage: www.elsevier.com/locate/matdes

Towards deeper carburizing by DEDp and L-PBF additive manufacturing of in-situ TiC-reinforced steel composites: powders and processability

Samuel El Haddaoui [a,b,*], Christophe Colin [b], Zehoua Hamouche [a], Sylvain Dépinoy [b], Cyril Gorny [a], Jorge Peixinho [a], Patrice Peyre [a]

[a] PIMM Laboratory, Arts et Métiers, CNRS, CNAM, Paris 75013, France
[b] Mines Paris, PSL University, MAT - Centre des Matériaux, CNRS UMR 7633, Versailles 78000, France

ARTICLE INFO

Keywords:
Additive manufacturing
Laser powder bed fusion
Direct energy deposition
Powder metallurgy
Metals

ABSTRACT

Additive manufacturing (AM) of iron-based metal matrix composites (IMMCs) enables the fabrication of more complex geometries than conventional processes for applications such as brake discs, transmission shafts, cutting tools, and gears. Current challenges associated with AM of IMMCs, including homogeneous reinforcement distribution and reinforcement/matrix interfacial decohesion, have been mitigated in the context of deep carburizing for gear applications.

In situ reinforcement by Laser Powder Bed Fusion (L-PBF) was achieved using nano-TiC (35–55 nm) dry coating onto spherical steel powder particles (15–45 μm) through Cyclomix® blade mixing, with a reinforcement content of 5 vol% (3.2 wt%). Powder rheology, powder density measurements, single-track experiments, high-speed imaging, and 3D builds revealed improved flowability due to coating, an increasing of spatters amount despite a low porosity rate (0.26 vol%).

Directed Energy Deposition using powder (DEDp) enables additional functionalities such as repair and compositional gradients while accounting for process-induced constraints. However, the powder must be coarser to ensure efficient stream. Turbula® premixed composite powders were used with spherical steel particles (45–125 μm) mixed and 3.2 wt% of micrometric TiC particles (3–8 μm and 15–30 μm). Video imaging, single-track experiments and 3D build showed that unmelted TiC particles could not be completely eliminated and create defects.

Hardening comparable to carburizing was achieved, increasing from 350 HV to 600 HV throughout the volume in L-PBF samples and at the surface in DED-p samples. Strengthening was likely induced by carbon diffusion from the reinforcement phase; however, the strong thermal cycling associated with DED-p caused softening in previously deposited layers.

1. Introduction

Thermochemically treated steels and carburizing steels such as those of the Böhler type exhibit high resistance to core crack propagation and high contact fatigue strength. However, current processes do not allow for hardened layer depths greater than 4 mm. Indeed, carbon diffusion kinetics are limited, and case-hardened parts must be exposed to high temperatures for extended periods to achieve deep hardening. This leads to a high risk of hot creeps and cracks. Yet, it is commonly admitted that the hardened layer must represent about 7 % of the part's thickness [1]. It is therefore challenging to produce large-dimension gears with carburized steels, for which the desired hardness level should reach a minimum of 550–600 $HV_{0.5}$ up to several millimeters in depth.

An alternative to such materials is iron-based metal matrix composites (IMMCs), where steels are reinforced with particles such as TiC that promote high hardness, low density, and exhibit excellent metallurgical compatibility with the matrix. The resulting composite exhibits desirable properties such as excellent wear resistance, high specific strength and relatively low production cost. Potential applications include cutting tools, drive shafts, brake disc, and gears subjected to severe friction and load conditions [1]. Manufacturing and forming these materials are nevertheless challenging through conventional means. In this framework, additive manufacturing appears as a promising way to process IMMCs.

* Corresponding author.
E-mail address: samuel.el_haddaoui@ensam.eu (S.E. Haddaoui).

https://doi.org/10.1016/j.matdes.2026.116439
Received 14 March 2026; Received in revised form 27 May 2026; Accepted 16 June 2026
Available online 17 June 2026

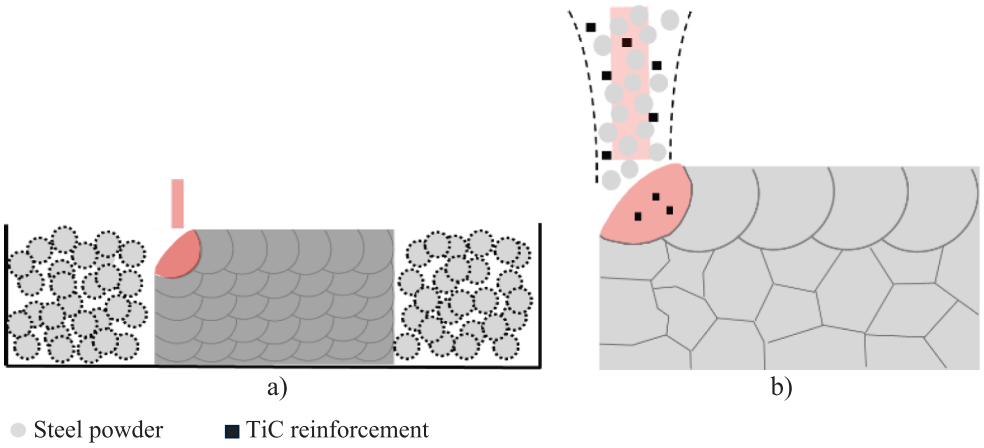

Fig. 1. Schematic representation of processing a 3.2 wt% TiC composite using a) dry coated nanoscale TiC by L-PBF and b) equivalent size particles blending for DEDp.

Indeed, additive manufacturing (AM) enables industrial production of complex parts, layer by layer, from a digital model. It offers great design freedom, reduces material waste, and allows for rapid and cost-effective production of prototypes or customized components. This technology opens new opportunities across various sectors, from aerospace to medicine, facilitating innovation and tailored manufacturing. Among the numerous existing AM processes, Direct Energy Deposition powder (DEDp) consists of injecting powder into a laser-induced melt pool. It allows local compositional changes during projection to create chemical gradients in build parts. The major advantage of this process is that it can be fabricated on a substrate that already has a complex geometry, enabling reparation of damaged parts. Another widely used process is Laser Powder Bed Fusion (L-PBF), where powder is deposited in successive layers and then locally melted by a laser, giving excellent geometric accuracy and good spatial resolution [2]. By combining these two processes, it would be possible to manufacture complex-shaped parts in IMMCs and locally add material to create compositional gradients or improve surface properties through DEDp refurnishing.

The industrial development IMMCs produced by additive manufacturing, particularly Laser Powder Bed Fusion (L-PBF), remains limited by several scientific and technological challenges. Among the main issues are:

1) achieving an homogeneous distribution of reinforcement particles, whose agglomeration promotes defect formation and deteriorates the overall mechanical properties,
2) controlling the matrix–reinforcement interface, which is essential to ensure efficient load transfer and limit particle debonding or pull-out phenomena,
3) Managing the temperature field, since the extreme melting and solidification rates induce porosity, cracking, residual stresses, and microstructural heterogeneities,
4) maintaining a satisfactory balance between mechanical strength and ductility, as the addition of reinforcements often reduces ductility [3].

To overcome these limitations, several research directions are currently being explored [3,4], with particular attention given to *in situ* synthesis processes and the development of new material compositions. *In situ* approaches appear especially promising for achieving a more homogeneous distribution of reinforcement phases and improving interfacial bonding through the controlled formation of carbides, nitrides, oxides, or intermetallic compounds directly during processing.

Low amounts of reinforcement facilitate processing and limit the risk of defects such as reinforcement agglomeration, interface decohesion, or cracking during cooling. Several authors have focused on the elaboration of these hypoeutectic composites, with TiC weight fractions below 3.8 wt% (according to the Fe–TiC pseudo-binary diagram). Higher reinforcement contents (up to 10 vol%) can significantly increase carbon and titanium dissolution during processing, thereby increasing the risk of cracking during the fusion process. In DEDp, although relatively large particles are used (≈ 50 μm on average), they remain small compared to the melt pool size (≈ 2 mm), allowing the deposition of a homogeneous powder mixture. As such, [5,6], fabricated parts using DEDp and highlighted carbon diffusion from the reinforcements into the matrix in low-alloy steel 16NCD13, with a hardness gradient comparable to case-hardened steels. However, the metallurgical quality was insufficient for mechanical testing. In work [7] similar materials in DEDp was used with higher reinforcement contents at 30 wt% to study tribological properties as a function of the cooling rate induced by the process. In both studies, the precipitation of TiC following its dissolution in the molten pool proved to be a critical factor. Indeed, the shape, size, and stoichiometry of TiC depended on the solidification and cooling rates.

For L-PBF processing of TiC-reinforced iron-based metal matrix composites (IMMCs), powder must exhibit chemical homogeneity at the particle scale because the metallic particle size (~30 μm) is comparable to the melt pool dimensions (~150–200 μm). Several powder fabrication routes have therefore been explored. Atomization enables the *in situ* formation of TiC during processing and produces spherical composite powders suitable for L-PBF, leading to significant matrix hardening and good densification; however, the process remains costly and difficult to adapt to new compositions due to the high melting temperature and low density of TiC compared with steel [6]. High-energy ball milling allows solid-state synthesis of composite powders but severely alters powder sphericity and introduces contamination risks from WC-Co milling media [9,10]. Low-energy ball milling reduces these drawbacks by embedding TiC particles onto spherical steel powders, although reinforcement dry coating efficiency remains limited and TiC agglomerates can generate cracking and lack-of-fusion defects during L-PBF [11,12,13]. Alternative powder metallurgy approaches, such as embedding [14] and chemical vapor deposition (CVD) [15], have also been investigated to improve reinforcement distribution while preserving powder morphology. Whereas spray drying agglomeration methods developed for laser cladding [16], demonstrate the possibility of producing stable composite granules with limited binder content.

In this context, nanometric TiC were coated onto spherical steel particles by Cyclomix® blade blending to promote *in situ* synthesis and homogeneous reinforcement repartition (Fig. 1a). The novelty of this approach lies in the use of a relatively high reinforcement fraction (5 vol %), whereas this powder mixing route is generally used with only 1 vol% of reinforcement [14]. This development opens new opportunities to easily explore a wide range of material compositions, including variations in reinforcement content, matrix alloy composition, and

Table 1
Chemical composition (wt. %) of steel powders after gas atomization measured by ICP and LECO elemental analyzer.

Wt. (%)	Fe	Ni	Cr	Mn	Si	Mo	C	P	S	O	N
Spec (NF A35-567)	Base	3.00 – 3.50	0.90 – 1.20	0.30 – 0.60	0.15 – 0.40	0.15 – 0.30	0.14 – 0.19	< 0.035	< 0.035	/	/
L-PBF	Base	3.20	0.96	0.48	0.23	0.27	0.14	< 0.005	< 0.005	0.018	0.003
DEDp	Base	3.20	0.98	0.48	0.24	0.28	0.15	< 0.005	< 0.005	0.007	0.003

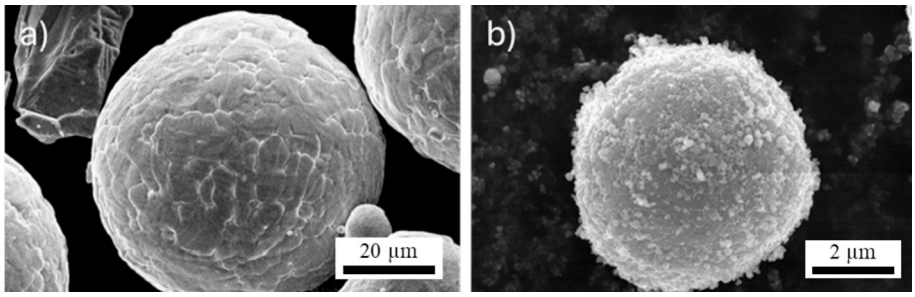

Fig. 2. Scanning electron microscope observations of powder blends: a) micrometric irregular-shaped TiC for DED-p, b) Batch 2 multilayer coated nano-TiC for L-PBF.

Table 2
Average chemical composition of the composite (in wt.%) before and after solidification by DEDp and L-PBF, measured by ICP mass spectrometry.

Process	Type	Alloying elements					Light elements			Contaminants			Base
		Ti	Cr	Mo	Mn	Ni	C	O	N	Si	S	P	
DEDp	Powder	2.4	0.94	0.26	0.46	3.1	0.63	0.029	0.05	0.22	<0.005	0.005	91.9
	Built	2.1	0.99	0.26	0.45	3.1	0.68	0.008	0.032	0.22	<0.005	0.005	92.1
L-PBF	Powder	2.5	0.94	0.26	0.46	3.1	0.70	0.380	0.067	0.22	<0.005	0.005	91.3
	Built	2.1	0.94	0.28	0.42	3.1	0.50	0.026	0.042	0.23	<0.005	0.005	92.3

reinforcement nature, while maintaining excellent metallurgical quality characterized by a homogeneous distribution of reinforcements and strong matrix–reinforcement interfacial cohesion. Such an approach offers significant potential for optimizing the mechanical and functional properties of these materials. A comparison with DEDp is also proposed, enabling the processing of IMMC's for applications where L-PBF is not suitable, such as part repair, compositionally graded materials, or localized reinforcement. However, the processing constraints associated with the projectability of the powder required the use of larger reinforcement particles (~30 µm), (Fig. 1b), which improve powder stream shape and stability without significantly increasing material cost.

2. Materials and methods

2.1. Powders preparation

Atomization was performed from an annealed 16NCD13 extruded billet (Ø: 150 mm, length: 1000 mm), followed by three sieving steps at 15, 45, and 125 µm. The chemical composition of the 16NCD13 case-hardening steel after atomization is presented in Table 1. The 15 – 45 µm distribution was used for L-PBF, and the 45 – 125 µm distribution for DEDp. Two powder batches were prepared for DEDp by mixing the steel powder with 3.2 wt% TiC using a Turbula® blender. Two TiC particle size distributions, either 15 – 30 µm or 3 – 8 µm in equivalent diameters,

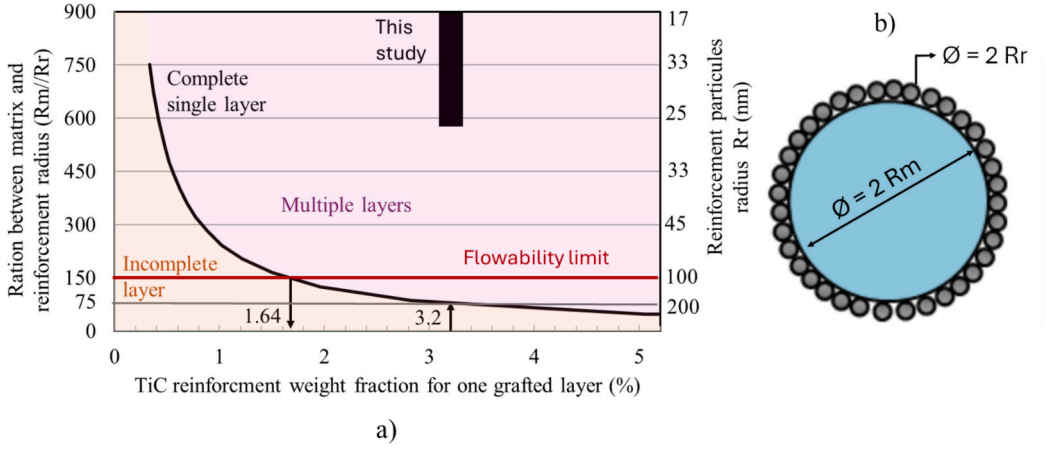

Fig. 3. (a) Calculation of Equations (1), 2 and 3 with a matrix particle diameter to be embedded of 30 µm, for one reinforcement layer thickness. Maximum limit of efficient ratio was defined as 150 from [14] (b) Schematic representation of the particle dry coating.

were considered to maximize their dissolution in the melt pool. The resulting mixture consists of spherical steel particles with grinded TiC characterized by irregular-shape (Fig. 2a). As a mean of comparison, unmixed steel powder was also used. For L-PBF, steel particles were blended with 3.2 wt% of 35——55 nm nanoparticles using a Cyclomix® system (Fig. 2b) at CEA-LITEN in Grenoble. Indeed, to maintain good powder flowability by dry coating, the ratio of matrix particle size to reinforcement particle size must be at least 150 [14]. Table 2 presents the quantified chimical composition before and after solidification.

As L-PBF powders have an optimal size range of approximately 15 to 45 μm, there exists a mean critical particle size of around 200 nm for the reinforcements below which embedding a single layer becomes hardly feasible. Indeed, assuming that the single layer completely covers the surface of the steel particles, the fraction of reinforcement is a function of particle size and can be estimate by (Equations (1) and (2) [16]:

$$N_r = 4 \times \left(\frac{R_m}{R_r}\right)^2 \tag{1}$$

$$V_r = \frac{Nr}{N_r + \left(\frac{R_m}{R_r}\right)^3} = \frac{1}{1 + \frac{1}{4}\left(\frac{R_m}{R_r}\right)} \tag{2}$$

$$W_r = \frac{V_r \rho_r}{V_r \rho_r + (1 - V_r)\rho_m} \tag{3}$$

Where V_r is the volume fraction of reinforcement, W_r weight fraction of reinforcement, N_r the number of embedded particles necessary to cover the whole surface of the base powder, R_m the radius of the particles to be embedded, R_r the radius of the reinforcement particles, ρ_r reinforcement bulk density and ρ_m matrix bulk density (Fig. 3b).

Fig. 3a shows that the weight fraction of reinforcement is limited to less than 2 wt% in the case of one reinforcement layer using (Eqs. (1), 2 and 3). To achieve a 3.2 wt% TiC, equivalent to a 5 vol%, it is necessary to embedded several layers of reinforcements, which correspond to dry coating. Thus, two different batches were processed with blade speeds of 8 m/s and 15 m/s, referred in the following as Batch 1 and Batch 2, respectively (Fig. 2b). Particle size distributions of dry coated powder were subsequently measured by granulomorphometry analysis. As in DEDp, the base steel powder was also used for comparison purposes.

2.2. Additive manufacturing tests

2.2.1. L-PBF tests

L-PBF single tracks were built to assess the effect of the properties of the composite powders on their processability. The machine used is an M2 Concept Laser equipped with an infrared laser operating at a wavelength of 1.07 μm. The spot diameter was set to 100 μm, and three different linear energy densities were selected (0.5, 0.33, and 0.25 J. mm^{-1}), using a constant power P, while varying the scanning speed V. The substrate, made of 16NCD13 steel, was 50 mm in diameter and 5 mm thick, with a rough sandblasted surface finish. Powder spreading was performed using a rubber scraper. Geometrical measurements of the consolidated single tracks were performed using a laser profilometer. The first measured parameter is the height dispersion H_{disp} as described in (Eq. (4)), where $\overline{H_{app}}$ is the mean track height and σ_H the standard deviation. It represents the dimensional stability of the track, which may oscillate or exhibit height fluctuations. Three domains can be identified based on height variation: a stable domain where the variation is below 25 %, a pinched domain where it falls between 25 % and 75 %, and a discontinuous domain where it exceeds 75 %.

$$H_{disp} = 100 \times \frac{\sigma_H}{\overline{H_{app}}} \tag{4}$$

The second parameter is the wetting angle θ between the substrate and the track. It was calculated from the height H_{app} and width e_{app} of the track using Equation (5).

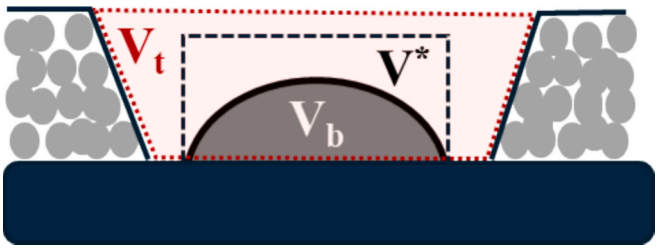

Fig. 4. 2D representation of a single-track cross-section after laser processing, illustrating the total volume (V_t), the volume built (Vb) and the volume of powder required for consolidation (V*).

$$\theta = 2 \times \arctan\left(2 \times \frac{H_{app}}{e_{app}}\right) \tag{5}$$

The last measured parameter, referred to as 'Build efficiency' (R_b), is the ratio between the volume of powder required for single track consolidation (V*) and the total volume (V_t), as illustrated in Fig. 4. Rb was calculated from optical profilometry measurements of the empty volume (V_e) and the built volume (V_b), according to Eq. (6). The relative density or compacity of the powder bed (C_{pb}) is determined, as defined using Eq. (11), as the ratio of the average of the apparent and tapped densities to the measured true density. The total volume (V_t) is the sum of the empty volume (V_e) and the built volume (V_b). The volume of powder required for single track consolidation (V*) is defined as the ratio of the built volume (V_b) and the compacity of the powder bed (C_{pb}).

$$R_b = \frac{V^*}{V_t} = \frac{V_b}{V_b + V_e} \times \frac{1}{C_{pb}} \tag{6}$$

Fast assessment of the effect of the powder layer thickness on processability was obtained by tilting the substrate, as describe by [17] and [18] at a 0,13° angle using a 200 μm aluminum foil and a 90 mm-diameter base. For a track length of 20 mm, this corresponds to a variation in powder thickness from 50 to 150 μm. The powder thickness was subsequently measured with a laser profilometer and assigned to the corresponding section of each single track. Based on the ratio between the height of the piston (40 μm) and the compacity of the powder (57 %), the representative height of the 3D constructions was calculated at 70 μm.

10 × 8 × 4 mm^3 3D specimens, corresponding to 100 layers in height, were produced by L-PBF. The laser spot size was set to 100 μm. After result from the single track study, four parameter sets were selected combining two linear energy densities: 0.25 and 0.5 J/mm, corresponding respectively to laser power – scanning speed couples of 200 W − 800 mm/s and 100 W − 200 mm/s.

Complementary L-PBF tests were carried out to quantify spatters on a test bench equipped with a 1 kW *redPOWER QUBE* laser (SPI Lasers), a 100 μm laser spot diameter, and an oxygen rate below 200 ppm inside the build chamber. The selected manufacturing parameters are equivalent to those of the industrial machine used for the fabrication of single tracks and 3D structures, namely a power of 200 W ± 20 W, a scanning speed of 0.8 m/s, and a 40 μm piston height. The high-speed camera used was a Fastcam Mini UX100, positioned at a grazing incidence relative to the build platform. Video acquisition was performed at 5000 fps with a resolution of 1280 × 1000 pixels. The videos were acquired under steady-state conditions, corresponding to the 30th layer, over a build of 11 × 11 x 1.2 mm^3. Image treatment was carried out using Fiji software, threshold between 60 and 255 pixels was applied to all images. The area (A) and perimeter (P) of each spatter represented by pixel cluster were then quantified and used for the calculation of the equivalent spherical diameter (D_{sph}) (Equation (7). Then sphericity index (I_{sph}) of each spatter was calculated using (Equation (8), an overestimation of the perimeter was observed for the smallest ejecta due to

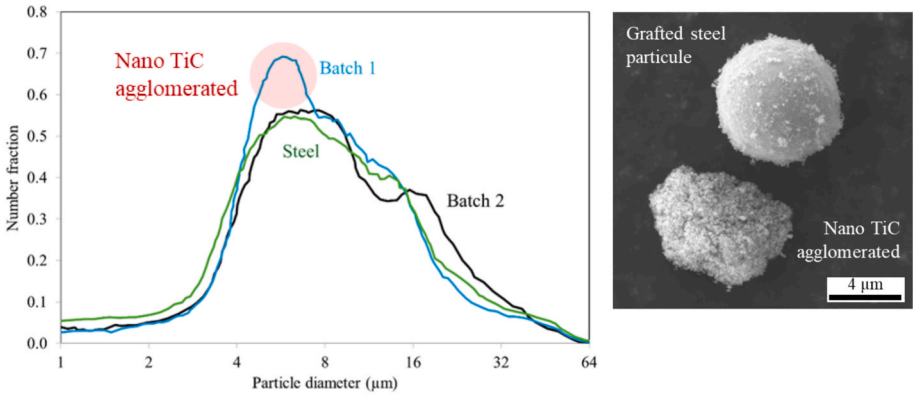

Fig. 5. a) Number-based particle size distribution measured using a granulomorphometer for L-PBF powders before and after mixing with the Cyclomix® at two blade speeds (Batch 1: 8 m/s and Batch 2: 15 m/s) and b) SEM micrograph of a micron-sized agglomerate composed of nanometric TiC observed in Batch 1.

limited discretization, resulting in a sphericity index lower than 1.

$$D_{sph} = \sqrt{\frac{4A}{\pi}} \tag{7}$$

$$I_{sph} = \frac{P}{D_{sph} \times \pi} \tag{8}$$

2.2.2. DEDp tests

DEDp single tracks were built to assess of the effect of processing parameters on the fraction of unmelted TiC particles. Indeed, a high concentration of reinforcement increases the risk of defects induced by their agglomeration. A large range of parameters such as laser power, speed, and spot size was tested. Two top-hat laser spot sizes of 2 and 3.2 mm were tested to increase the melt pool width at equivalent laser intensity. The powder feed rate was fixed at 6 g/min, and three scanning speeds were tested: 200, 400 and 600 mm/min. The working distance was set to 13 mm, which corresponds to the focal planes of both the powder stream and the laser stream. Cross sections of single tracks were then polished and the surface fraction of unmelted particles was analyzed by image treatment. The quantified surface fraction was converted into a weight fraction for comparison with the initial TiC ratio of 3.2 wt%. Only the first blend including TiC with diameters of 15 to 36 µm was tested.

For DEDp, 4 mm-high builds, corresponding to 5 deposited layers, were produced on 30 × 30 mm^2 steel substrates. The process parameters were as follows: the laser power was set to 1300 W, the scanning speed to 400 mm/min, and the powder feed rate to 6 g/min, based on single-track studies to provide a good compromise between reinforcement dissolution and good track geometry for improved processability. The same 0/90° scan strategy was selected for both processes, with an overlapping ratio of 20 to 30 %.

DEDp powder streams were analyzed using video imaging and a laser sheet method. Particles were projected within the nozzle and reflected the radiation from a 2D laser grid. This reflection was recorded by high-speed cameras, and each spot was associated with a particle. The laser sheet was moved in upwards increments of 0.5 mm with an acquisition frequency of 196 images per second over 2 s. This allows observation of the projected surface distribution of particles. Spatial distributions of the powder jet along the symmetry axis of the nozzle were thus reconstructed for three powder batches.

3. Results

3.1. Analysis of powders and powder rheology

3.1.1. L-PBF powder rheology

The compactness and flowability of the powders were assessed using the Carr index I_C and Hausner ratio R_H (Eqs. (9) and (10). To this aim, the apparent density ρ_a and the tapped density ρ_t were measured using a tapped density tester at 300 taps per minute until the volume stabilized. Furthermore, the apparent and tapped powder compacities C_a and C_t were determined using (Eq. (11), with the true density ρ_{true} was measured with a helium pycnometer.

$$R_H = \frac{\rho_t}{\rho_a} \geq 1 \tag{9}$$

$$I_C = \frac{\rho_t - \rho_a}{\rho_t} \times 100 \tag{10}$$

$$C_i = \frac{\rho_i}{\rho_{true}} \tag{11}$$

Where the index *i* denotes either the apparent or tapped density.

In addition, powder shear cell tests were carried out to characterize the flowability of the coated powders under conditions similar to L-PBF recoating. An annular cell is attached to an Anton Paar Modular Compact Rheometer (MCR) 502 able to control the normal force. The annular metallic cup has an outer diameter of 45 mm, an inner diameter of 19 mm, and a height of 14 mm. The sample volume is 18.9 mL. The bottom of the cell is corrugated and the cover attached to the rheometer is an annular plate (outer diameter 42 mm and inner diameter 21 mm) with 12 fins of 2 mm thickness to avoid slippage at the walls. The cell was gently filled with the powder, then the top surface was flattened using a scraper bar, hence avoiding tapping. The sample is first over-consolidated at high normal stress (3 kPa) under static conditions, then the normal stress is reduced and a low shear rate corresponding to 5.10^{-3} rotation per minute is applied through the top plate. The measured shear stress τ_c at the moment of the avalanche is obtained for different normal stresses σ_n. By plotting Mohr's circles (Fig. 6), it is possible to determine the compressive strength σ_c and the major consolidation stress σ_1, and use them to calculate the flowability index f_f, (Equation (12). Two tests were performed on the same L-PBF steel powder, and one test was carried out for each dry coated batch. The statistical robustness of the flowability index reported for Batch 1 and Batch 2 is therefore limited, and these values should be interpreted as indicative rather than statistically representative.

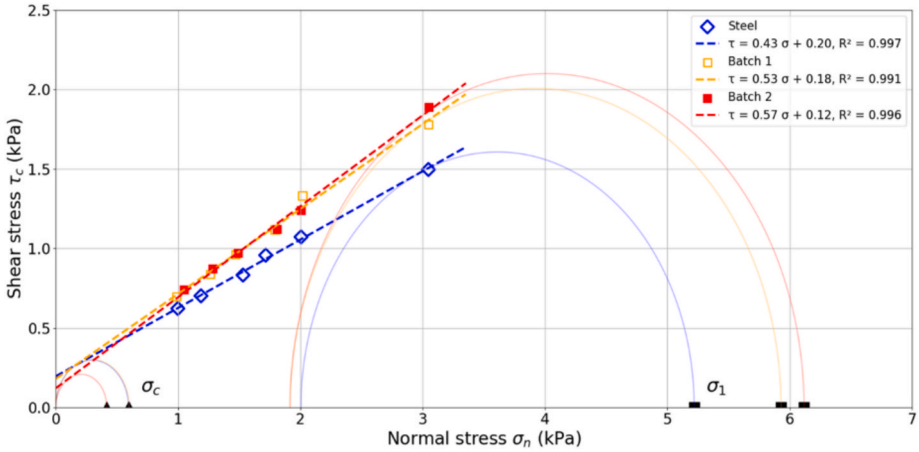

Fig. 6. Plots of Mohr's circles obtained from the Powder Rheology Tests with: σ_c compressive strength, σ_1 major consolidation stress used for f_f flowability index calculation.

Table 3
Results of densities, compacities, Hausner ratio, Carr index and the rheology in shear stress condition for L-PBF powders with: σ_1 the major consolidation stress, σ_c cohesive stress between particles, f_f flowability index.

	ρ_{true} (g/cm^3)	ρ_a (g/cm^3)	ρ_t (g/cm^3)	C_a	C_t	Hausner ratio	Carr index (%)	σ_1 (Pa)	σ_c (Pa)	f_f
Steel	7.85	4.45	5.14	0.57	0.65	1.16	13.4	5219	595	8.8
Batch 1	7.61	4.09	5.01	0.54	0.66	1.22	18.4	5929	600	9.9
Batch 2	7.58	4.23	4.90	0.56	0.65	1.16	13.7	6117	417	14.7

$$f_f = \frac{\sigma_1}{\sigma_c} \tag{12}$$

Particle size distribution of the L-PBF dry coated powder shows an overpopulation of particles around 5 μm in diameter for Batch 1. In contrast, for Batch 2, the size of the largest particles (around 20 μm) increases significantly. SEM observations also show agglomerates with sizes comparable to the smallest steel particles (Fig. 5). The blade speed of 8 m/s was thus insufficient to achieve complete dry coating of the nanoparticles, unlike Batch 2, which was carried out with a larger rotation speed of 15 m/s. The nanometric reinforcements were therefore able to stack in multiple layers on the surface of the spherical steel particles.

Density measurements led to a Hausner ratio and Carr index similar for the three considered powders, although Batch 1 which increased above 1.2 and 15 % indicating a lower flowability mainly due to a lower apparent density (Table 3). For rheological test result, flowability index (f_f) categorizes powders as free flowing ($f_f > 10$), easy flowing ($4 < f_f < 10$), difficult flowing ($2 < f_f < 4$), or non-flowing ($f_f < 2$) [19,20]. In the present case, f_f is equal to 8.8 for the only steel powder and increases to around 9.9 for Batches 1, corresponding to easy flowing, and 14.7 for Batch 2 corresponding to free flowing. This result is due to the increase of dry coated powders slope curve, which indicates decrease of frictional forces between the particles by dry coating. In addition, a significant decrease in the cohesion stress was observed for batch 2, indicating that a lower force is required to break the cohesive forces between particles to initiate their flowing.

By combining the two methods, it can be deduced that complete dry coating improves the flowability of the particles by reducing the friction forces between them under shear stress. Poor mixing conditions lead to the formation of TiC nanoparticle agglomerates, which deteriorate the powder flowability. Therefore, only Batch 2 is considered in the following.

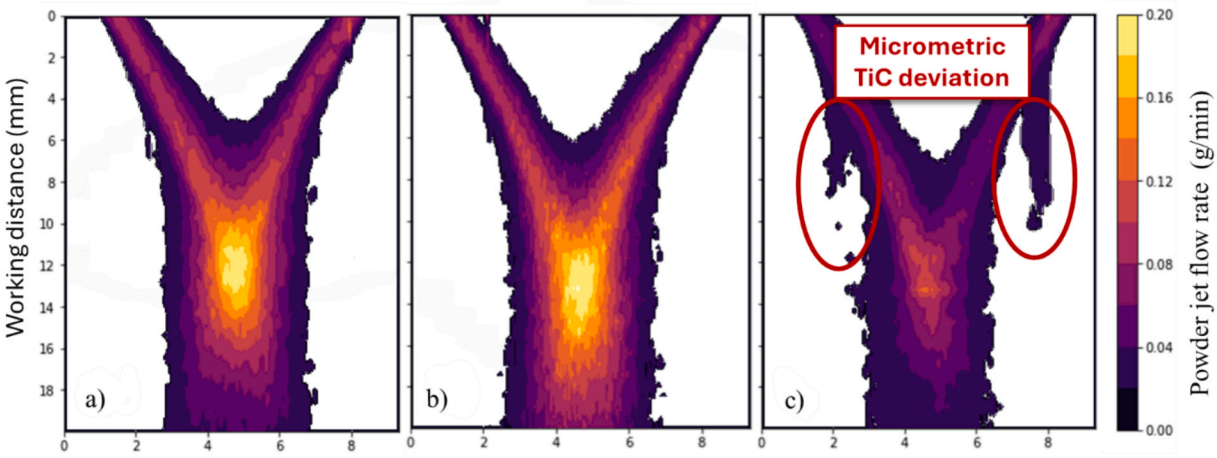

Fig. 7. Powder jet flow rate as a function of position from the nozzle (mm) for three powders a) steel; b) steel + 3,2 wt% TiC (d10: 15 μm, d90: 36 μm) c)) steel + 3,2 wt% TiC, (d10: 2 μm, d90: 8 μm).

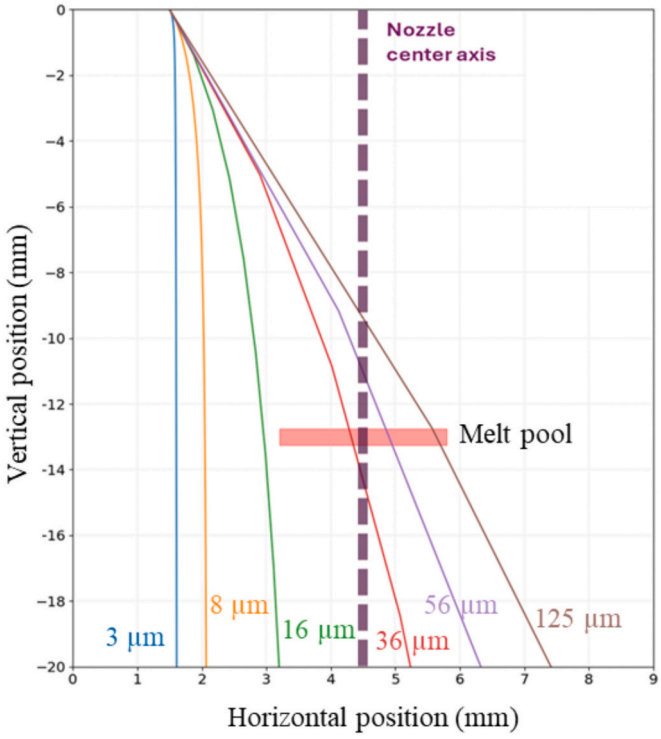

Fig. 8. Result of TiC particles projection calculated using Lagrange's law.

3.1.2. Analysis of DEDp powder stream

When compared to powder flowability in L-PBF, the first relevant parameter concerning powder feeding stability in DEDp is the shape of the powder stream. Fig. 7 shows the powder jet flow rate for the three investigated powders. Distance between the outer nozzle and the powder focal plan is between 11 and 14 mm, with a diameter of 2.8 mm, considered at $1/e^2$ (14 %) of the Gaussian peak value. The powder jet of micrometric reinforcements exhibits a shorter trajectory than the steel particles (Fig. 7c and a, respectively). Indeed, in that case, the drag force certainly surpassed the kinetic energy of the fine and lighter particles, which could not be capted by melt pool. The ability to be capted appears to be more favorable for TiC particle sizes around 20 µm, corresponding to Fig. 7b. However, it's important to note that laser sheet imaging captures the projected surface of the particles. As such, the distribution in terms of surface fraction overrepresents the small particle population compared to their mass or volume fraction. Even a few percent of micrometric reinforcement particles can have a significant impact on the flow rates measured by laser sheet technique. Thus, a numerical assessment of the effect of the TiC particle size on their trajectory during projection was conducted using Lagrange's law. A more detailed description of this model is given in [5]. Calculations were carried out by launching particles using (Eqs. (13), 14 and 15), assuming spherical TiC particles launched from a fixed point at a 60° angle relative to the vertical axis which experienced no collision. The central carrier gas is argon, and both the velocity and angle of the particles at the nozzle exit are considered.

$$\frac{d\overrightarrow{V_p}}{dt} = \overrightarrow{a_{drag}} + \overrightarrow{P} = \frac{3\rho_g C_d}{4\rho_p d_p}\left|\overrightarrow{V_g} - \overrightarrow{V_p}\right|\left(\overrightarrow{V_g} - \overrightarrow{V_p}\right) + \overrightarrow{g}\frac{\rho_p - \rho_g}{\rho_p} \quad (13)$$

$$C_d = \frac{24}{Re_p} \times (1 + 0,179\,Re_p^{0.5} + 0,013\,Re_p) \quad (14)$$

$$Re_p = \frac{\rho_p d_p \left|\overrightarrow{V_p} - \overrightarrow{V_g}\right|}{\mu} \quad (15)$$

Where $\overrightarrow{V_p}$ is the velocity vector of the particle, $\overrightarrow{V_g}$ the velocity vector of the carrier gas, ρ_g the density of the carrier gas, ρ_p the density of the particle, d_p the particle diameter, C_d the drag coefficient [5,21], $\overrightarrow{g}$ the gravity acceleration, Re_p the Reynolds number for particles and µ dynamic viscosity of argon.

Results are shown in Fig. 8 and from parameters Table 4, where the size of the melt pool was taken as 2.5 mm, an order of magnitude typical of the DEDp process. These calculations are in good agreement wih the experimental observations: while particles of diameters comprised between 36 and 125 µm ended in the melt pool, particles of 3 to 8 µm are strongly deflected during projection. According to the Lagrange's law, as the particle size increases, the drag force decreases. Conversely, when the particle size decreases, there exists a critical diameter below which the drag force becomes too large for the particle to reach the melt pool. The destabilization of the powder jet observed in Fig. 7c is thus likely due to the deceleration of the smaller particles that fall far from the center of the powder stream. In the following, only the powder mixture with 15–36 µm is used.

3.2. Analysis of single tracks

3.2.1. Single L-PBF tracks

Single tracks of steel powder and Batch 2 powder were analyzed at two powder layer thicknesses, respectively, 70 µm and 130 µm. Considering height dispersion as a relevant parameter, similar stability domains are observed for both powders at the lower powder thickness. The most stable domain corresponds to a linear energy range of 0.33 to 0.5 J/mm and a power range of 200 to 300 W (Fig. 9). Humping appears at high scanning speeds, above 1000 mm/s, while balling is significant at low power levels, around 50 W. For thicker powder thicknesses, a lower dispersion is observed with the steel powder, whereas the stability domains remain similar for batch 2 powder (Fig. 10). This suggests that powder characteristics may influence processability, particularly for the thicker powder layers.

The effect of processing parameters for a powder layer thickness of 70 µm on the wetting angle and build efficiency is shown in Figs. 11 and 12, respectively. It is generally assumed that the keyhole regime exhibits a low angle, below 40°, while the conduction regime results in angle ranging between 50° and 60°, and the balling phenomenon is characterized by an angle greater than 60° [18]. Differences are observed between steel and dry coated powders in the typical keyhole domain between 250 W and 350 W at high linear energy densities. In this range, the wetting angle is greater than 75° for steel and below 40° for the composite (Fig. 11). The near-keyhole regime appears to be destabilized by dry coating. This difference can be explained by the drop in build efficiency for all power levels and scanning speeds (Fig. 12). A possible explanation is the occurrence of more spatters from dry coated powders, which are visually detected during building. Such spatters depend on the melt pool temperature and the vapor plume / melt-pool friction and can be affected by the keyhole regime [22]. Two low-efficiency domains can be identified: the first between 100 and 150 W, and the second at high scanning speeds above 1000 mm/s. For the study of 3D builds, two

Table 4
Input parameters for the calculations of Fig. 8.

Initial particle velocity Vp (m/s)	Angle between $\overrightarrow{g}$ and $\overrightarrow{V_p}$ (°)	Gas velocity Vg (m/s)	Gas density (kg/m^3)	Particles density (kg/m^3)	Gravity (m/s^2)	Argon dynamic viscosity µ (Pa.s)
2.5	30	6	1.78	4910	9.81	2.2×10^{-5}

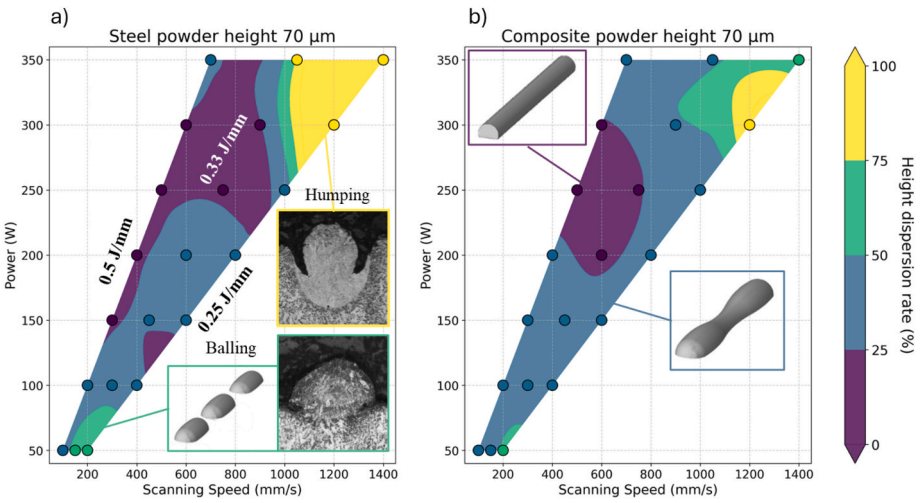

Fig. 9. Height dispersion rate H_{disp} of single track as a function of the scanning speed and laser power for a powder thickness of 70 µm: a) steel and b) batch 2 composite.

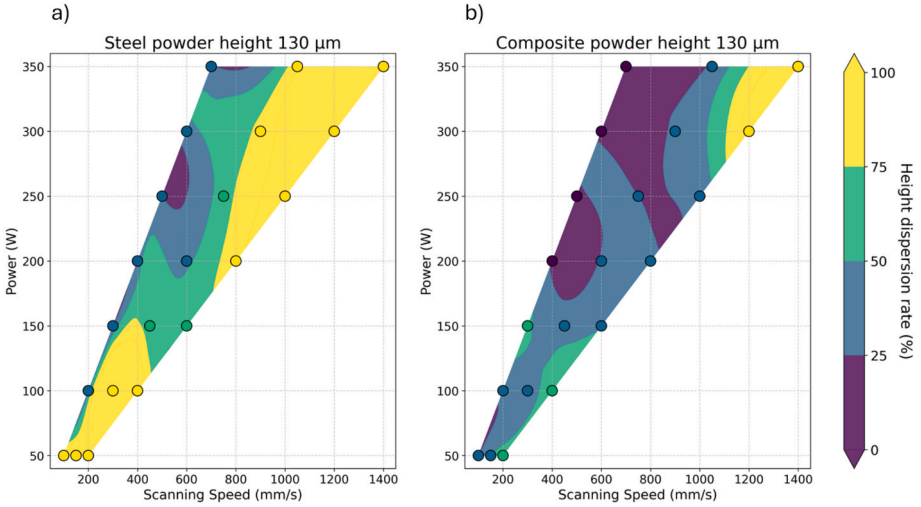

Fig. 10. Height dispersion rate H_{disp} of single track as a function of the scanning speed and laser power for a powder thickness of 130 µm: a) steel and b) batch 2 composite.

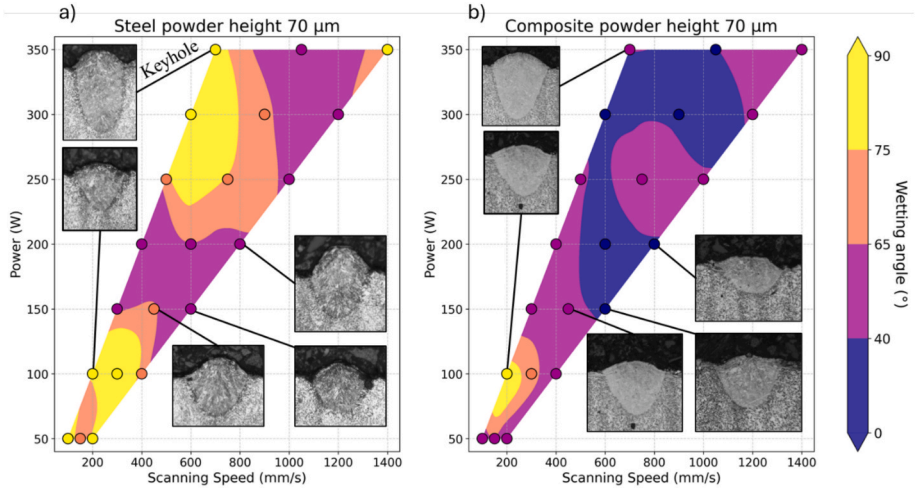

Fig. 11. Wetting angle θ of single track as a function of the scanning speed and laser power for a powder thickness of 70 µm: a) steel and b) batch 2 composite.

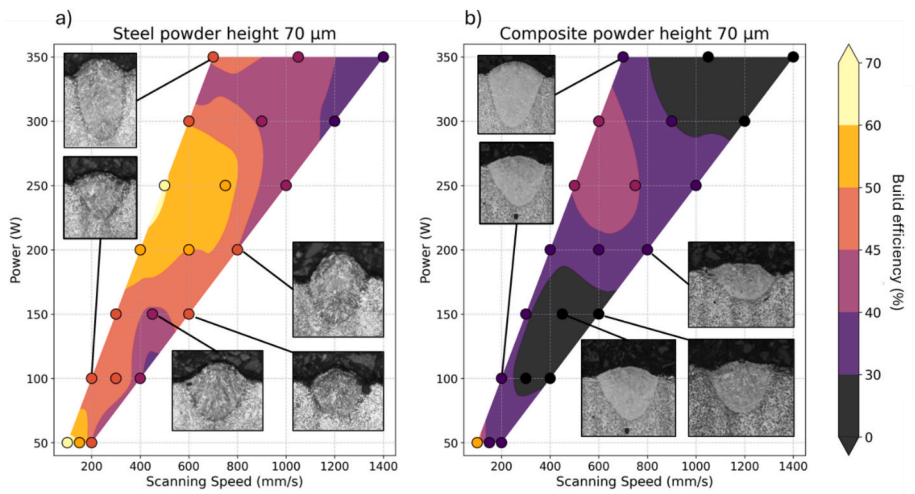

Fig. 12. Build efficiency R_b of single track as a function of the scanning speed and laser power for a powder thickness of 70 µm: a) steel and b) batch 2 composite.

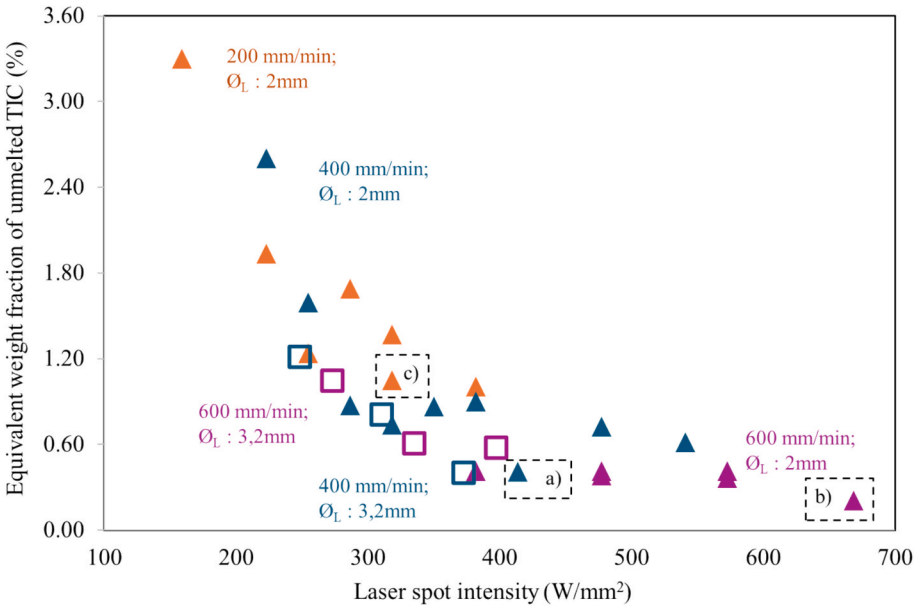

Fig. 13. Mass fraction of unmelted TiC particles as a function of laser intensity for two top-hat spots sizes $\varnothing_L$ of 2 mm and 3.2 mm, and three scanning speeds of 200, 400 and 600 mm/min.

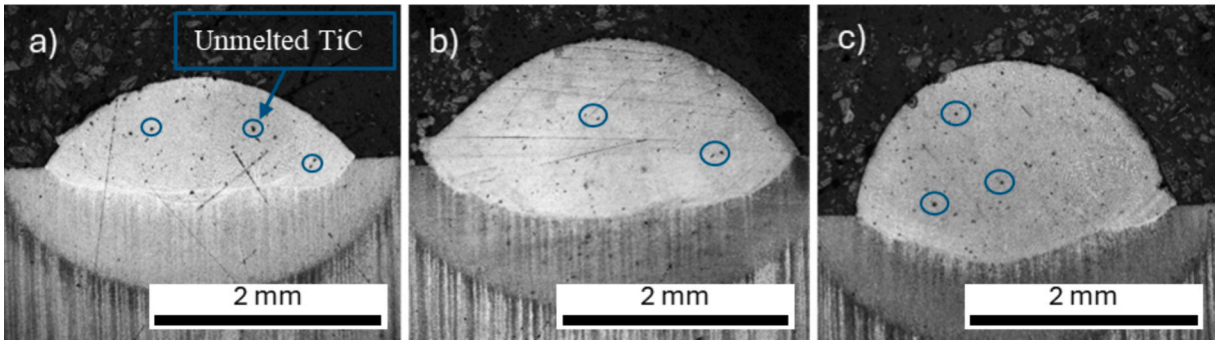

Fig. 14. Optical micrography of DEDp single track sections, a) 1300 W, 400 mm/min, 6 g/min, $\varnothing_L = 2$ mm; b) 2100 W, 600 mm/min, 12 g/min, $\varnothing_L = 2$ mm; c) 1000 W, 200 mm/min, 6 g/min, $\varnothing_L = 2$ mm top hat.

parameter sets with different linear energy densities were selected based on this study: 100 W – 200 mm/s and 200 W – 800 mm/s. The hatch spacing values were calculated from the single-track widths obtained for a powder layer thickness corresponding to the steady-state regime

Table 5
L-PBF process parameters used for 3D build composite and 16NCD13 steel.

	Power (W)	Scanning speed (mm/s)	Hatch spacing (μm)	Overlap rate (%)	Piston height (μm)
P1	100	200	114	20	40
P2	100	200	100	30	40
P3	200	800	102	20	40
P4	200	800	89	30	40

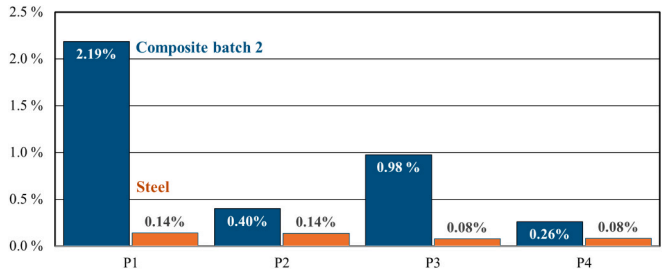

Fig. 15. Porosity rates measured by image analysis after polishing for batch 2 composite and steel.

defined like the piston displacement divided by the powder compacity. Two overlap rates were selected, 20 % and 30 %, to investigate their effects on the porosity rate (Table 5).

3.2.2. Single DEDp tracks

The fraction of unmelted TiC particles (initially with a particle size distribution of 15 – 36 μm) shows a strong correlation with the laser intensity. An exponentially decreasing trend (Figs. 13 and 14) is observed that reaches an asymptotic limit of unmelted TiC around 0.3—0.4 wt%. Typical single tracks are shown in Fig. 14, with micrometric unmelted particles clearly visible. This is probably due to the low dissolution kinetics of the larger TiC particles (50 μm) in the liquid steel. Increasing the laser spot diameter $\varnothing_L$ from 2 mm to 3.2 mm extends the width of the melt pool, but its effect on TiC dissolution remains negligible compared to the influence of laser intensity. Moreover, the mass flow rate and the scanning speed affect the material feed rate more than the melt pool temperature, so their influence is therefore limited. As the power range is limited due to the heating of the printing nozzle at high energy, this means that full dissolution of TiC particles appears hardly feasible.

3.3. Analysis of 3D parts: melt-pool stability, defects and hardness profiles

3.3.1. Chemical composition

The average chemical composition of the composite was measured by ICP and LECO mass spectrometry (Table 2). The reinforcement fraction initially used was 3.2 w.% for both processes representing 2.5 w. % of Ti and 0.64 w. % for C. Approximately 30 % of the carbon content (from 0.7 to 0.5 wt%) is lost during L-PBF processing, probably due to reactions with oxygen originating from powder moisture (0.38 wt % O in the dry coated powder, which decreases to 0.026 % after L-PBF). This oxygen content indicates a high sensitivity of the dry coated powders to moisture, likely caused by the high specific surface area induced by the nano-TiC coating. It is also likely that the packaging conditions prior to shipment for chemical composition analysis contributed to this effect, as the container was not sufficiently protected against humidity. In DEDp, the powder mixture is less homogeneous because of the risk of powder sedimentation, which led to greater scatter in the results. The powder does not exhibit significant moisture content, and no significant carbon loss is observed after solidification.

3.3.2. Analysis of 3D L-PBF parts

Based on the previous characterizations, 3D parts were built using the steel and Batch 2 powders with four different sets of parameters, summarized in Table 5. Porosity rates obtained with the composite powder are higher than only steel powder (Fig. 15). However, a reasonable surface porosity level of 0.26 % could be achieved using the set of parameters P4 (Table 5). Fig. 16 shows an optical observation of the specimen built with this set of parameters. Porosities are located at the junctions between multiple tracks and are due to lack-of-fusion, either caused by spatters or instability in the melt pool width, which prevents a constant overlapping between adjacent tracks. However, the geometrical accuracy is maintained with parameter set P4, and no cracks are observed. After chemical etching, the last layer exhibits a different microstructure compared to the previous layers. Otherwise, optical analysis does not reveal any macroscopic heterogeneities, and no defects related to the use of reinforcement, such as agglomerated or

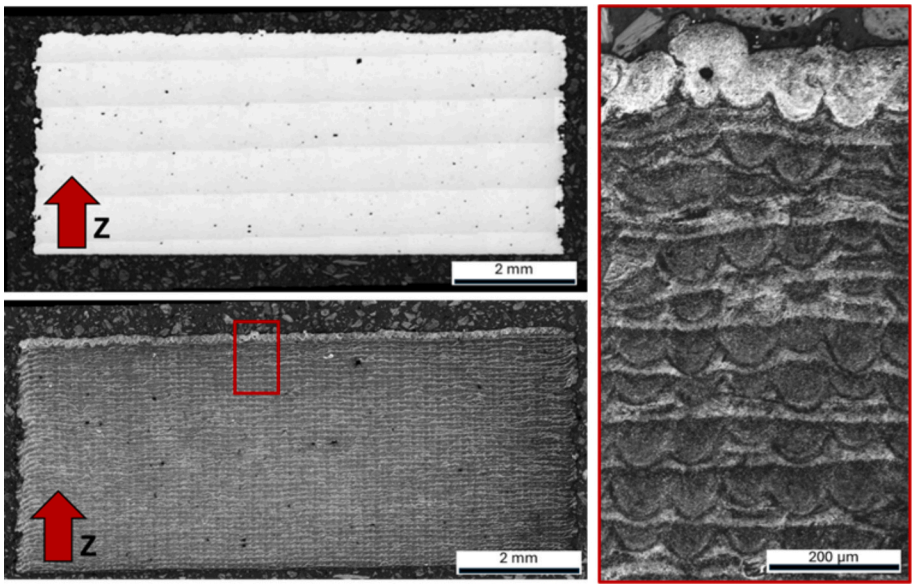

Fig. 16. Optical micrography before and after Nital etching of sample P4 (200 W, 800 mm/s), produced by L-PBF using dry coated composite powder (Batch 2), showing a measured porosity of 0.26 %.

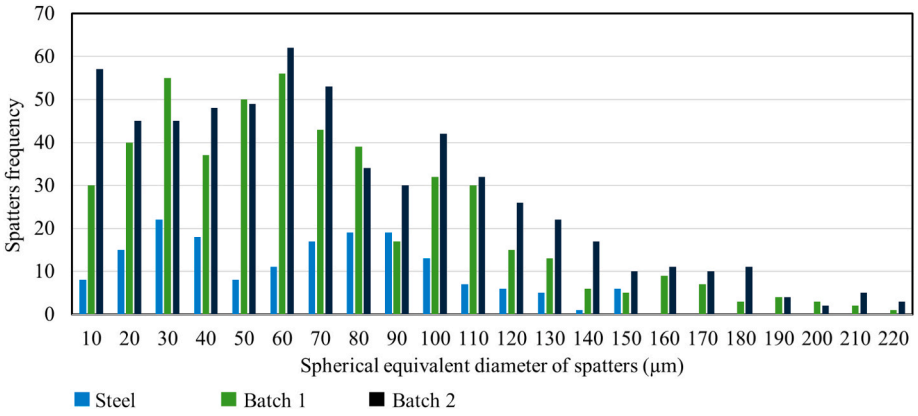

Fig. 17. Size distribution of spatters using spherical equivalent diameter for three powders: only steel, Batch 1 dry coating using a Cyclomix® blade speed of 8 m/s, and Batch 2 at 15 m/s.

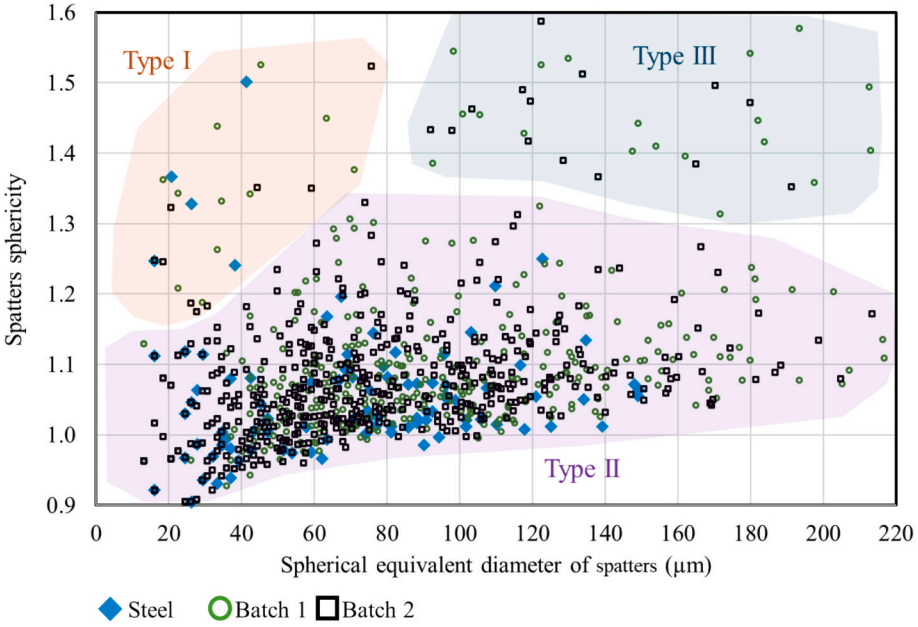

Fig. 18. Sphericity versus size for each spatter with three powders: only steel, Batch 1 dry coatedusing a Cyclomix® blade speed of 8 m/s, and Batch 2 at 15 m/s. The three types are of spatter highlighted: (I) interacted with the metallic vapor, (II) droplets emitted from the melt pool, and (III) ejecta originating from powder ejected from the front of the melt pool [24].

unmelted TiC particles, are observed.

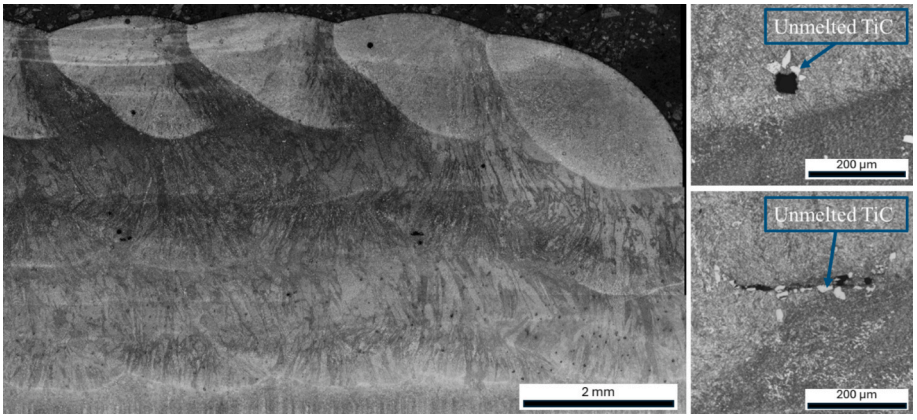

Fig. 19. Optical micrograph of the steel/TiC composite produced by DEDp, etched with Nital, showing defects due to the agglomeration of unmelted particles and microstructural heterogeneities.

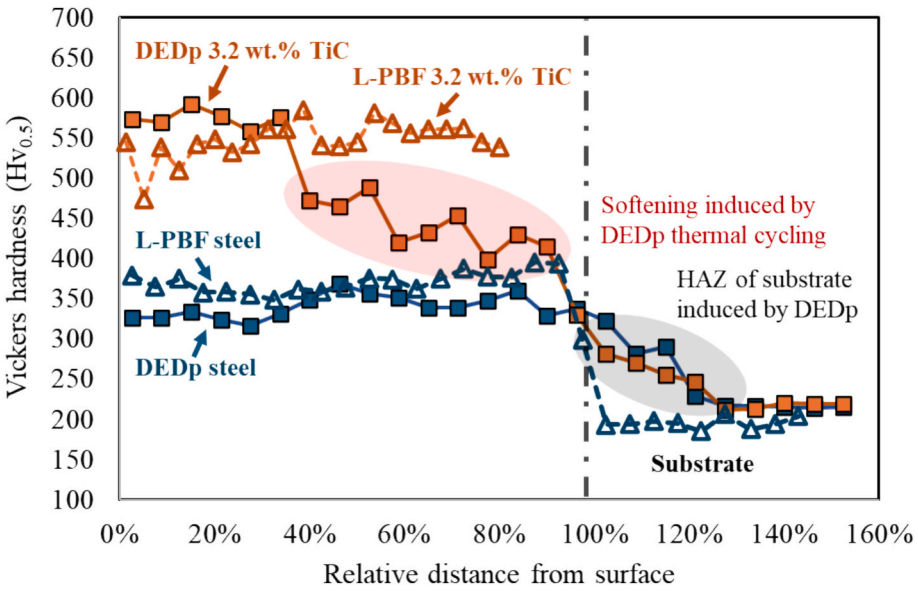

Fig. 20. Vickers hardness profiles from top of the build (0 %) to the 16NCD13 annealed substrate (>100 %) for a build height of 4 mm (composite vs steel, and DEDp vs L-PBF).

3.3.3. Analysis of spatters during L-PBF builds

The analysis of spatters provides useful information on the melt-pool/surrounding powder bed stability [23,24]. Approximately five times more spatter was quantified with the addition of dry coated TiC nanoparticles (Fig. 17), over a diameter range of 10 to 220 μm. These spatters mainly originate from molten metal ejected from the melt pool, caused by instabilities. Three types of spatter are highlighted in Fig. 18: (I) spatter that interacted with the metallic vapor; these particles are small and deformed due to the recoil pressure from the vapor plume, (II) droplets emitted from the melt pool, which represent the majority of the ejecta, with a wide size range (including large ones above 150 μm) and good sphericity, and (III) ejecta originating from powder expelled from the front of the melt pool; these particles have a size equal to or larger than the powder particles and exhibit an irregular shape [25].

When comparing the only steel to dry coated powder (Fig. 18), a population of spatters larger than 150 μm and highly deformed appears for the dry coated powders. These spatters are attributed either to strong melt pool instabilities or to particle agglomerates that fail to penetrate the melt pool from its front. Another cause would be the reduction in surface tension induced by the change in chemical composition, which would affect the stability of the melt pool.

3.3.4. Analysis of DED builds

In contrast, the hypoeutectic 3D samples produced by DEDp (at 1300 W, 400 mm/min and 6 g/min using 2 mm in diameter 'top hat' laser spot) exhibit defects related to the addition of reinforcements. Optical micrographs after chemical etching with Nital reveal agglomerations of unmelted TiC particles (Fig. 19). These agglomerates lead to porosity or cracking within the steel matrix. Microstructural heterogeneities are observed in the top layer, where a martensitic microstructure is identified which is then thermally affected by subsequent layers, as already reported in martensitic steel processed by DEDp [26,27]. The previous layer also appears to have been tempered during the deposition of subsequent layers.

3.3.5. Hardness tests (L-PBF vs DEDp samples)

Hardness measurements were made using a Vickers indenter with a 500 g load. Hardness profiles started from the surface and extended toward the substrate of the fabricated parts with a step of 250 μm for DEDp and 150 μm for L-PBF. Reported values are the average of three profiles. The parts were subsequently polished using standard metallographic preparation procedures, and porosity was quantified by optical image analysis with a pixel area of 1.2 μm^2 over the entire surface, using two sections oriented at 0° and 90° relative to the build axis. In a final procedure, a 4 vol% Nital etching was used to reveal the solidification tracks to locate the defects and determine their origin. SEM observations were performed on a ZEISS Sigma 300 (FEG) at 5 kV.

Fig. 20 shows a comparison between the hardness profiles of the composites and steels processed by DEDp and L-PBF, expressed as a function of the relative distance to the substrate, where 0 % and 100 % corresponds respectively to the surface of the top layer and to the substrate. The substrate material is 16NCD13 steel in the annealed state, exhibiting a hardness of approximately 200 HV. Steels exhibit a similar and constant hardness of around 350 HV throughout the whole part, although the L-PBF specimen seems to be slightly harder. This is likely due to the microstructural refinement caused by the higher solidification rates for L-PBF process. On the other hand, the composites are harder, although there are differences between the two processes. Indeed, the top-surface of the DEDp specimen, consisting of fresh martensite reinforced with TiC particles, exhibits a hardness of 550 to 600 $HV_{0.5}$, which then drops from 550 up to 350 $HV_{0,5}$ in the previously built layers due to the intense thermal cycling that likely causes precipitation of large TiC and tempering of the matrix. The part produced by L-PBF, on the other hand, exhibits a hardness of 550—600 HV over the entire building height. This high hardness is likely due to the marked dissolution of TiC nanoparticles, leading to carbon diffusion into the matrix and subsequent precipitation of sub-stoichiometric TiC during cooling.

When comparing these hardness values with those reported in the literature for similar materials, a significant effect of alloying elements on the matrix can be observed. 16NCD13 steel was processed by DEDp and observed a similar hardness gradient, reaching 600 HV in the final layer with 5 wt% TiC reinforcement [5]. Pure iron matrix was employed with the same TiC content, processed by LPBF; however, the resulting hardening remained moderate at 357 HV and was mainly attributed to grain size refinement [8]. For martensitic stainless steel AISI 420, it was reported that hardening up to approximately 600 HV, also with 5 wt% TiC reinforcement [13]. It is thus likely that presence of carbide-forming elements such as chromium and molybdenum promotes the precipitation of mixed carbides with lower carbon content, which can diffuse into and strengthen the matrix.

As such, while both processes were able to produce IMMCs with hardness comparable to case-hardened steels, the L-PBF process appears

to be the most promising one for building parts with high hardnesses over several millimeters in depth.

4. Conclusion

High-speed blade mixing has proven effective for producing composite powders with TiC nanoparticles dry coated onto spherical steel particles. At high blade rotation speeds (15 m/s), high amounts of TiC nanoparticles (5 vol%) can be coat in multiple layers without forming agglomerates, maintaining or even improving flowability and compacity under shear stress conditions. However, dry coating increases denudation and spatters during L-PBF, influencing the melt pool stability and the wetting behavior of deposited tracks. A low porosity rate of 0.26 % was obtained with fine and homogeneous L-PBF microstructures. Hardness increases in volume at a level similar to case-hardened steel (600 $HV_{0.5}$).

In contrast, DEDp is limited by the minimum particle size (~10 μm) that disallows a good projection. This limits the complete dissolution of TiC in the melt pool. Thermal cycling significantly decreases hardness in the previously built layers probably due to lower carbon content in the matrix caused by strong TiC precipitation during solidification. Furthermore, agglomerates of unmelted reinforcements can cause defects and microstructural heterogeneities.

Multiples layers nanoparticles dry coating offers a cost-effective alternative to atomization for producing composite powders with high reinforcement content while preserving powder processability. These findings provide insight into melt pool physics, powder–laser interaction, and the mechanisms governing denudation, spatter, and wetting angles. High reinforcement content coatings can be achieved in DEDp for wear-resistant applications, while L-PBF process ensures fine and homogeneous microstructures. No cracks were observed in any of the parts produced during this study for both processes. However, the limited quantity of composite powder available did not allow the production of large-dimension parts, in which residual stress effects would likely become more critical. Fabrication of complex geometries may induce local stress concentrations and generate additional risks of cracking. These aspects therefore require further investigation in future studies. Furthermore, heat treatments can be designed to optimize carbon distribution and TiC precipitation, improving machinability or hardness.

CRediT authorship contribution statement

Samuel El Haddaoui: Writing – original draft. **Christophe Colin:** Supervision. **Zehoua Hamouche:** Investigation. **Sylvain Dépinoy:** Investigation. **Cyril Gorny:** Resources. **Jorge Peixinho:** Resources. **Patrice Peyre:** Supervision.

Declaration of competing interest

The authors declare that they have no known competing financial interests or personal relationships that could have appeared to influence the work reported in this paper.

Acknowledgement

This work was funded by the French Defence Innovation Agency (AID) and the GIS HEAD (Scientific Interest Group dedicated to high-energy additive manufacturing processes). The authors acknowledge the technical platform at Univ. Grenoble Alpes, CEA, Liten, DTNM for the dry coating of TiC nanoparticles using blade blender. The authors also acknowledge the EPROM platform (Elaboration, Procédés & Matériaux) at Mines Paris – PSL University, CMAT – Centre des Matériaux, for providing access to the industrial L-PBF machine used for the additive manufacturing experiments.

Data availability

Data will be made available on request.

References

[1] Leroux, C., 2011. «Cémentation par le carbone et carbonitruration - Mise en œuvre des traitements» Techniques de l'ingénieur Matériaux | Traitements des métaux, M1226 V2, 2011.
[2] M. Ostolaza, J.I. Arrizubieta, A. Lamikiz, S. Plaza, N. Ortega, Latest Developments to manufacture metal matrix composites and functionally graded materials through AM: a state-of-the-art review, Materials 16 (4) (2023) 1746, https://doi.org/10.3390/ma16041746.
[3] Y. Fang, M.-K. Kim, Y. Zhang, Z. Duan, Q. Yuan, J. Suhr, 2022. «Particulate-reinforced iron-based metal matrix composites fabricated by selective laser melting: a systematic review. J. Manufacturing Process.» 74 (2022) 592–639 633 https://doi.org/10.1016/j.jmapro.2021.12.018.
[4] S. Chen, S. Chu, B. Mao, «Iron-based metal matrix composite: a critical review on the microstructural design, fabrication processes, and mechanical properties», Acta Metallurgica Sinica (english Letters) 38 (2025) https://doi.org/10.1007/s40195-024-01758-1.
[5] Novichenko, D., 2011. « Fabrication par projection laser et caractérisation des pièces en composites a base d'acier et carbure de titane» 2011 PhD thesis manuscript.
[6] N. Richardeau, C. Colin, K. Vieillevigne, 2010. 'Fabrication et caractérisation de matériaux avancés (Nicomic C263 et 16NCD13/TiC) mis en œuvre par projection laser pour l'industrie aéronautique' internship report 2010.
[7] A. Emamian, M. Alimardani, A. Khajepour, Effect of Cooling Rate and Laser Process Parameters on Additive Manufactured Fe–Ti–C Metal Matrix Composites Microstructure and Carbide Morphology, J. Manuf. Process. 16 (4) (2014) 511–557, https://doi.org/10.1016/j.jmapro.2014.07.002.
[8] A. Perminov, G. Bartzsch, A. Franke, H. Biermann, O. Volkova, Manufacturing Fe–TiC composite powder via inert gas atomization by forming reinforcement phase in Situ, Adv. Eng. Mater. 23 (3) (2021) 2000717, https://doi.org/10.1002/adem.202000717.
[9] B. AlMangour, D. Grzesiakb, J.-M. Yang, Nanocrystalline TiC-reinforced H13 steel matrix nanocomposites fabricated by selective laser melting, Mater. Des. 96 (2016) 150–161, https://doi.org/10.1016/j.matdes.2016.02.022.
[10] L. Jaworska, A. Olszowka-Myalska, S. Cygan, P. Figiel, M. Karolus, J. Cyboron, 'The influence of tungsten carbide contamination from the milling process on PCD materials oxidation' Int, J. Refract. Met. Hard Mater. 64 (2017) 60–65, https://doi.org/10.1016/j.ijrmhm.2017.01.008.
[11] E. Fereiduni, A. Ghasemi, M. Elbestawi, Characterization of composite powder feedstock from powder bed fusion additive manufacturing perspective, Materials 12 (2019) 3673, https://doi.org/10.3390/ma12223673.
[12] C. Li, X. Deng, Y. Li, Z. Wang, Adding Cr and Mo simultaneously enhances the strength and impact toughness of TiC microparticle-reinforced steel matrix composites at high temperatures, J. Alloy. Compd. 931 (janvier) (2023) 167531, https://doi.org/10.1016/j.jallcom.2022.167531.
[13] Y. Liu, M. Tang, Hu. Qi, Y. Zhang, L. Zhang, Densification Behavior, Microstructural Evolution, and Mechanical Properties of TiC/AISI420 Stainless Steel Composites Fabricated by Selective Laser Melting, Mater. Des. 187 (février) (2020) 108381, https://doi.org/10.1016/j.matdes.2019.108381.
[14] M. Soulier, A. Benayad, L. Teulonb, Y. Oudart, S. Senol, K. Vanmeensel, Nanocomposite powder for powder-bed-based additive manufacturing obtained by dry particle coating, Powder Technol. 404 (2022) 117474, https://doi.org/10.1016/j.powtec.2022.117474.
[15] T. Babul, M. Baranowski, Sobczak, M. Homa, W. Lésniewski, 2016. « Thermophysical properties of cu-matrix composites manufactured using Cu powder coated with graphene. » J. Mater. Eng. Perform. 2016, 25, 3146–3151. DOI: 10.1007/s11665-016-2174-5.
[16] X. Zhang, S. Pfeiffer, P. Rutkowskie, M. Makowska, D. Kata, J. Yang, T. Graule, 2020. « Laser cladding of manganese oxide doped aluminum oxide granules on titanium alloy for biomedical applications» Applied Surface Science 520 (2020) 146304, https://doi.org/10.1016/j.apsusc.2020.146304.
[17] D. Marcos, M.-H. Berger, C. Colin, 2018. « Développement de MOULes INNOVants à haute conductivité thermique pour l'injection de matières plastiques fabriquées par Selective Laser Melting (SLM/LBM)». THÈSE DE DOCTORAT de l'Université de recherche Paris Sciences et Lettres PSL Research University MINES ParisTech.
[18] P. Vinson, Y. Bienvenu, C. Colin, 2020. « Fusion sélective par laser de lits de poudre : Étude sur le recyclage de la poudre et détection de défauts au cours de la fabrication par imagerie thermique ». THÈSE DE DOCTORAT de l'Université de recherche Paris Sciences et Lettres PSL Research University MINES ParisTech.
[19] K. Saleh, P. Guigon, 2012. « Mise en œuvre des poudres - Stockage et écoulement des silos » Techniques de l'ingénieur, Procédés chimie - bio - agro | Opérations unitaires. Génie de la réaction chimique, Réf. : J2255 V1, 2012.
[20] J. Zegzulka, D. Gelnar, L. Jezerska, R. Prokes, J. Rozbroj, Characterization and flowability methods for metal powders, Sci. Rep. 10 (1) (2020) 21004, https://doi.org/10.1038/s41598-020-77974-3.
[21] M.V. Kravtsov, Resistance to the free steady-state motion of a sphere in a viscous medium, J. Eng. Phys. 15 (3) (1968) 833–888, https://doi.org/10.1007/BF00826653.

[22] M.J. Matthews, G. Guss, S.A. Khairallah, A.M. Rubenchik, P.J. Depond, W.E. King, Denudation of metal powder layers in laser powder bed fusion processes, Acta Mater. 114 (Aug. 2016) 33–42, https://doi.org/10.1016/j.actamat.2016.05.017.
[23] V. Gunenthiram, P. Peyre, M. Schneider, M. Dal, F. Coste, R. Fabbro, 'Analysis of laser–melt pool–powder bed interaction during the selective laser melting of a stainless steel', J. Laser Appl. 29 (2) (May 2017) 022303 https://doi.org/10.2351/1.4983259.
[24] G. Chebil, P. Lapouge, Y. Renollet, C. Davoine, M. Thomas, V. Favier, M. Schneider 'Study of spatter ejections during laser-powder bed fusion process for aluminum alloys' J. Laser Appl. 33, 042047 Volume 33, Issue 4, 2021 https://doi.org/10.2351/7.0000493.
[25] D. Wang, S. Wu, F. Fu, S. Mai, Y. Yang, Y. Liu, C. Song, Mechanisms and characteristics of spatter generation in SLM processing and its effect on the properties, Mater. Des. 117 (Mar. 2017) 121–130, https://doi.org/10.1016/j.matdes.2016.12.060.
[26] H.-K. Kang, H. Lee, C.-S. Oh, J. Yoon, Microstructure and mechanical properties of laser direct energy deposited martensitic stainless steel 410, Micromachines 15 (2024) 837, https://doi.org/10.3390/mi15070837.
[27] A. Roy, A. Dhal, R. Jain, P. Agrawal, B.A. Shreya Mukherjee, C.M. McWilliams, K. C. Cho, R.S. Mishra, Heterogenous phase evolution and mechanical response in additively manufactured low alloy martensitic steel processed via laser-directed energy deposition, Materials & Design 243 (2024) 113060, https://doi.org/10.1016/j.matdes.2024.113060.